PHOTONICS Research

High-resolution two-photon transcranial imaging of brain using direct wavefront sensing

Congping Chen,[1,2,3,†] Zhongya Qin,[1,2,3,†] Sicong He,[1,2,3] Shaojun Liu,[4,5] Shun-Fat Lau,[2,6,7] Wanjie Wu,[1,2,3] Dan Zhu,[4,5] Nancy Y. Ip,[2,6,7] and Jianan Y. Qu[1,2,3,*]

[1]Department of Electronic and Computer Engineering, The Hong Kong University of Science and Technology, Clear Water Bay, Kowloon, Hong Kong, China
[2]State Key Laboratory of Molecular Neuroscience, The Hong Kong University of Science and Technology, Clear Water Bay, Kowloon, Hong Kong, China
[3]Center of Systems Biology and Human Health, The Hong Kong University of Science and Technology, Clear Water Bay, Kowloon, Hong Kong, China
[4]Britton Chance Center for Biomedical Photonics, Wuhan National Laboratory for Optoelectronics, Huazhong University of Science and Technology, Wuhan, China
[5]MoE Key Laboratory for Biomedical Photonics, Collaborative Innovation Center for Biomedical Engineering, School of Engineering Sciences, Huazhong University of Science and Technology, Wuhan, China
[6]Division of Life Science, The Hong Kong University of Science and Technology, Clear Water Bay, Kowloon, Hong Kong, China
[7]Molecular Neuroscience Center, The Hong Kong University of Science and Technology, Clear Water Bay, Kowloon, Hong Kong, China
*Corresponding author: eequ@ust.hk

Received 20 January 2021; revised 14 March 2021; accepted 14 March 2021; posted 16 March 2021 (Doc. ID 420220); published 1 June 2021

Imaging of the brain in its native state at high spatial resolution poses major challenges to visualization techniques. Two-photon microscopy integrated with the thinned-skull or optical clearing skull technique provides a minimally invasive tool for *in vivo* imaging of the cortex of mice without activating immune response and inducing brain injury. However, the imaging contrast and spatial resolution are severely compromised by the optical heterogeneity of the skull, limiting the imaging depth to the superficial layer. In this work, an optimized configuration of an adaptive optics two-photon microscope system and an improved wavefront sensing algorithm are proposed for accurate correction for the aberrations induced by the skull window and brain tissue. Using this system, we achieved subcellular resolution transcranial imaging of layer 5 pyramidal neurons up to 700 μm below pia in living mice. In addition, we investigated microglia–plaque interaction in living brain of Alzheimer's disease and demonstrated high-precision laser dendrotomy and single-spine ablation.

https://doi.org/10.1364/PRJ.420220

1. INTRODUCTION

Direct visualization and manipulation of neurons, glia, and microvasculature in their native environment is crucial to understanding how the brain functions. With the growth of fluorescent protein and transgenic technology, two-photon excited microscopy has become an indispensable tool for *in vivo* brain imaging of small rodents over recent decades because of its high spatial resolution and optical-sectioning capability [1,2]. However, the biggest obstacle for direct imaging of the brain in a living animal is the opaque skull because it attenuates both the excitation and emission photons of two-photon microscopy severely, yielding poor image quality even in the superficial brain region.

The primary methods of providing optical access to the mouse brain are the open-skull and thinned-skull protocols [3,4]. The major limitation of open-skull approach is that skull removal will inevitably trigger the glia-mediated inflammatory reaction and disturb the neuronal physiology [5,6]. Although an exceedingly thin (~20 μm) skull could provide an imaging resolution close to that with an open-skull window at the superficial layer, the probability of mechanical disruption of cortex and activation of neuroinflammation is high, and optical access is restricted to a very small area [4]. To minimize the risk of brain trauma and inflammation, skull can be mechanically thinned to a certain thickness (~50 μm) to effectively reduce the scattering while holding its structural integrity to protect the underlying brain and produce a large field of imaging up to ~4 mm^2 [7]. Alternatively, optical clearing technique can improve the skull transparency by degrading the collagen fibers and removing the inorganic minerals with chemical reagents [8–10]. However, aberrations arising in optical heterogeneity in the mechanically thinned or chemically cleared skull hamper transcranial brain imaging performance in both resolution and depth.

Adaptive optics (AO), originally developed for astronomical telescopes, has been introduced recently to improve two-photon microscopy by correcting system- or sample-induced aberrations [11,12]. The wavefront aberrations can be determined by either direct [13–17] or indirect [18–20] methods. The direct wavefront sensing approach employs a Shack–Hartmann wavefront sensor (SHWS) to measure the wavefront distortion using the two-photon excited fluorescence signal inside the specimen or so-called guide star. Wang *et al.* employed the descanned and laterally averaged two-photon excited guide star in the visible wavelength range to recover near-diffraction-limited imaging in zebrafish larval brains [14]. They further extended this approach to more opaque mouse brain by using a near-infrared (NIR) guide star generated by exogenous dye that was directly injected into the brain [15]. Recently, Liu *et al.* improved this approach by creating guide star signals from NIR dye within microvessels [16]. The direct wavefront sensing approach is fast, robust, and photon efficient, enabling two-photon imaging of layer 5 neurons through an open-skull cranial window [15,16], and its imaging depth through the thinned-skull window reached ~500 μm below the pia [16]. In this work, we developed AO two-photon microscopy for high-resolution cortical imaging through both thinned-skull and optical clearing skull windows (Fig. S1 in Ref. [21]). We built an ultrasensitive SHWS incorporating a microlens array and an electron-multiplying charge-coupled device (EMCCD) to measure the wavefront of a descanned two-photon excited fluorescent (TPEF) guide star. The wavefront distortion was fed to a deformable mirror (DM) to introduce a compensating distortion to the excitation light, correcting the aberrations. We optimized the excitation numerical aperture (NA) of the microscope system, which alleviated the scattering of the excitation laser and also extended the depth of direct wavefront sensing. We advanced the wavefront sensing algorithm by averaging the Shack–Hartmann images from arbitrarily distributed near-infrared (NIR) guide stars in a three-dimensional (3D) subvolume, allowing the reliable determination of aberration beneath the skull window and brain tissue. Using this system, we first characterized the optical properties of the skull windows and then achieved *in vivo* neuronal imaging in mouse brains with much improved spatial resolution and signal intensity up to ~700 μm below pia. We then investigated the interaction between microglia and plaque in a mouse model of Alzheimer's disease (AD). Taking advantage of the tight focus provided by AO correction, we demonstrated precise laser-mediated dendrotomy and single-spine ablation of layer 5 pyramidal neurons, and we studied the microglial dynamic response to this neuronal microsurgery.

2. RESULTS

A. Wavefront Sensing: System Optimization and New Algorithm

Accurate measurement of wavefront distortion in deep tissue imaging is particularly challenging because the scatterings from brain tissue and skull deteriorate the SHWS image of the TPEF guide star and cause error of wavefront sensing. Here we propose an AO two-photon microscope system for transcranial brain imaging by underfilling the back aperture of a high-NA objective [Fig. 1(a)]. The effective NA for excitation path and wavefront sensing was optimally reduced to mitigate optical scattering of a fluorescent guide star signal and enable direct wavefront sensing in the deep brain region. After wavefront measurement and correction, a flipping dichroic mirror (D2) directed the TPEF signal to the imaging channel, and the full NA of the objective was then used for fluorescence collection (Fig. S1 in Ref. [21]). Although reducing excitation NA has been proved advantageous for improving both confocal and two-photon imaging of scattering tissues [22–24], its utility in direct wavefront sensing has not been demonstrated. To examine the effectiveness of this approach, we conducted Monte Carlo simulation to evaluate the performance of wavefront sensing under different effective NA conditions (Fig. S2 in Ref. [21]). Specifically, we modelled how the guide star fluorescence propagates through a two-layer scattering medium resembling brain/skull tissues and finally reaches the SHWS (details in Section 4.F). The results showed that, with the same amount of photons collected by the SHWS, the signal-to-background ratio (SBR) of the guide star images on SHWS was significantly increased when reducing the effective NA {Fig. 1(b), Figs. S2b and S2c in Ref. [21]}. This is attributed to the rejection of TPEF photons entering the objective at higher angle, which experience stronger scattering because of their longer path length of light–tissue interaction [Fig. 1(b)]. Next, we reconstructed the wavefront using the simulated SHWS images and plotted the wavefront errors as a function of effective NA at various imaging depths [Fig. 1(c)]. As expected, the reduction of effective NA is beneficial to the accuracy of wavefront measurement, especially in the deep region, because the light beyond the aperture of reduced effective NA that contributes to most of the errors in wavefront measurement is rejected [Fig. 1(b)]. It was found that the configuration of effective NA at 0.7 produces a good balance between wavefront sensing accuracy and diffraction-limited resolution [Fig. 1(c)]. To verify the simulation results, we conducted *in vivo* imaging of yellow fluorescent protein (YFP) labelled neurons in Thy1-YFP mice through a thinned-skull window of 50 μm thickness using the overfilled and underfilled configurations. The effective NA of the underfilled configuration was set to 0.7. As shown in Figs. 1(d) and 1(e), and Fig. S3 in Ref. [21], the quality of the SHWS images was greatly improved by reducing the NA for excitation and wavefront sensing, consistent with the simulation conclusions. Furthermore, the two-photon excited fluorescence intensity was enhanced up to twofold when reducing the excitation NA from 1.05 to 0.7 (Fig. S4 in Ref. [21]), in agreement with a study of the open-skull preparation [24]. In the rest of this work, we adopted the underfilled configuration with effective NA of 0.7 to improve the accuracy of direct wavefront sensing as well as the efficiency of two-photon excitation. Although we show that the strategy of reducing excitation NA is most helpful for sensor-based AO, sensorless approaches could also benefit from the decreased scattering of excitation laser and enhancement of signal intensity in deep tissue imaging. We also labelled the microvasculature with Evans blue through retro-orbital injection into mice to generate an NIR guide star and increase the

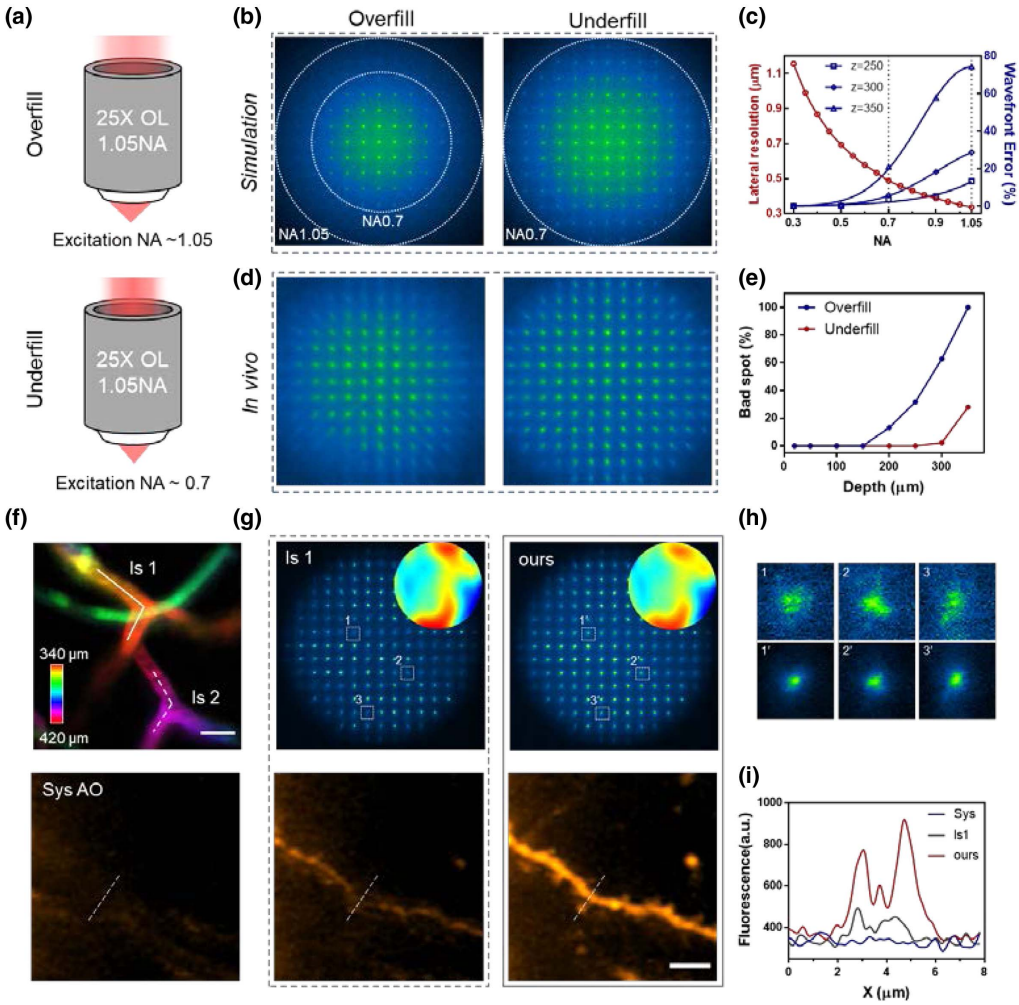

Fig. 1. Optimization of the excitation NA and improved wavefront sensing algorithm. (a) Schematic illustration of a high-NA objective in the overfilled (top) and underfilled (bottom) configuration. (b) Monte Carlo simulated SHWS images from the guide star at 250 μm below the thinned skull with full NA and reduced NA of the objective. The dashed circles indicate the apertures for the effective NA of 1.05 and 0.7, respectively. Details are shown in Fig. S2 in Ref. [21]. (c) Simulated wavefront errors and theoretical lateral resolution as functions of effective NA. (d) Representative guide star images of YFP fluorescence in Thy1-YFP mice when the objective was overfilled (left) and underfilled (right) at 250 μm below the thinned skull. Details are shown in Fig. S3 in Ref. [21]. (e) Percentages of bad spots in the Shack–Hartmann spot image for overfilled (blue) and underfilled (red) configurations. A bad spot is the one with poor signal quality (SBR less than 1.2) to make its center unidentifiable. (f) Top: depth-coded images of the NIR-dye labelled microvascular vessels for direct wavefront sensing. Two segments of vessels at different depths (solid line and dashed line labelled with ls 1 and ls 2) were line scanned for wavefront measurement. Scale bar: 10 μm. Bottom: two-photon images of YFP labelled dendrite with system correction only. (g) Top row: guide star images on the SHWS with only ls 1 (left) and our algorithm (right). The right-top corners display the corresponding corrective wavefronts. Bottom row: the corresponding AO corrected images. Details are presented in Fig. S7 in Ref. [21]. Scale bar: 5 μm. (h) Comparisons of the detailed structures of the numbered spots in (g). (i) Intensity profiles along the dashed lines in the bottom panel of (f) and (g).

depth of direct wavefront sensing as reported in previous work [15,16].

Since the skull is highly heterogeneous and induces large aberrations, we characterized the optical aberrations induced by the thinned-skull window alone in an *in vitro* preparation. We created a 3D tissue phantom by dispersing fluorescent beads (0.2 μm in diameter) in a mixture of Evans blue/agarose and then placing a piece of isolated thinned skull (50 μm in thickness) on top of the sample. Evans blue fluorescence provided bright and uniform guide stars for direct measurement of the aberrations of the thinned-skull window, while the fluorescent beads were used to evaluate the point spread function (PSF) distortion caused by the aberrations. Because the wavefront distortion varies spatially due to the skull heterogeneity, we first investigated the isoplanatic field of view (FOV) within which the aberrations were similar. We performed AO corrections by averaging the aberrations over a series of FOV ranges and compared the enhancement of the fluorescence intensity of the central bead (Fig. S5 in Ref. [21]). As can be seen, the aberrations would average out when the guide star was scanned over a too large field, while if the scanned field is too small, tissue scattering yields irregular Shack–Hartmann spots and induces errors in determining the aberration [14]. The optimal scanning FOV was found to be a square with sides of 30–60 μm (Fig. S5b in

Ref. [21]). Further, we characterized the aberrations of the thinned-skull window at various depths (Fig. S6 in Ref. [21]). The results showed that AO increased the fluorescence intensity up to tenfold and restored near-diffraction-limited resolution over 600 μm below the skull.

Next, we applied the AO approach to *in vivo* imaging of the mouse cortex in Thy1-YFP mice with Evans blue retro-orbitally injected to label the brain vasculature to serve as the guide star in the deep brain region. To measure the aberrations, we excited the labelled microvessels in ~60 μm × 60 μm and integrated the descanned fluorescence signal on the SHWS. However, a large number of spots in the SHWS image exhibited irregular and asymmetrical patterns, even when the guide star signals were obtained from scanning over a few segments of blood vessel {Figs. 1(f) and 1(h), and Fig. S7 in Ref. [21]}. This induced errors in spot center identification and wavefront measurement, resulting in inaccurate or incomplete AO correction. The phenomenon may be caused by the high-order aberrations from the optical heterogeneity of skull/brain tissue and shadowing of blood vessel(s) from upper layers of tissue [14,15]. The errors cannot be sufficiently reduced by averaging the guide star signal in one imaging plane. Given that an isoplanatic correction is valid within a small 3D volume [16,25], not merely in a 2D focal plane, we developed a wavefront reconstruction algorithm by averaging the SHWS images captured at different depths within the isoplanatic volume and then spatially filtering each spot with its neighbors (details in Section 4). This approach yields a significantly clearer SHWS image, and single spots stand out in each cell of the sensor, enabling more accurate aberration determination [Figs. 1(g)–1(i)]. By using this algorithm, we reliably corrected the aberrations and greatly improved the imaging performance {Figs. 1(g)–1(i), and Fig. S7 in Ref. [21]}. Although the AO correction was based on the averaged SHWS images over adjacent depths, we did not observe any degradation of correction performance in each layer. In principle, as long as the guide star signal is integrated in a volume smaller than the isoplanatic patch, the average process provides a better spot pattern in the averaged SHWS image for aberration measurement and does not compromise AO performance. It should be noted that this approach improves the correction accuracy by sacrificing certain correction speed. Specifically, the major time consumption is the integration of all guide star signals at different depths. The integration times for the averaged SHWS images in different experiments are summarized in Table S1 in Ref. [21]. In principle, this method is not limited to the skull windows. It is also applicable to other imaging conditions where the heterogeneity of biological tissues causes errors in wavefront measurement. The 3D average of guide star signals will be essential to reduce the spatial-variant high-order aberrations.

B. Structural and Functional Imaging of Brain Cortex through the Thinned-Skull Window

Taking the advantage of the optimized imaging system and new algorithm of wavefront sensing, we conducted *in vivo* transcranial imaging of cortex through a thinned skull of ~50 μm thickness in Thy1-YFP mice. As can be seen, even with system aberration corrected, the neuronal dendrites and somata were severely blurred by aberrations caused by skull and brain tissue [Figs. 2(a) and 2(b)]. With full AO correction, however, pyramidal neurons spanning hundreds of micrometers in depth could be resolved clearly, along with the surrounding microvessels. Quantitative comparisons show that AO not only dramatically enhanced the fluorescence intensity but also recovered the optimal subcellular resolution at depths as great as 680 μm below the pia {Figs. 2(a)–2(c), and Fig. S8 in Ref. [21]}. These results lead to the conclusion that AO is essential and efficient for high-resolution and deep-brain imaging through minimally invasive thinned-skull windows.

Next, we applied the AO two-photon microscopy to functional calcium imaging of somatosensory neurons in a transgenic mouse line (CaMPKII-GCaMP6s) through the thinned-skull window [Fig. 2(d)]. As can be seen, the spontaneous fluorescence signal from the neuronal somata at over 340 μm below pia was noticeably increased after full AO correction. More importantly, full AO correction recovered the calcium transients of dendritic compartments due to its much enhanced resolution, which otherwise could not be distinguished from the background noise or so-called "neuropil contaminations" [26] [Figs. 2(d) and 2(e)]. Although our AO correction is based on direct wavefront sensing of the NIR guide star from microvessels and independent of the labeling density of cellular structures, the depth of functional calcium imaging is smaller than that of the structural imaging. This is mainly due to the large out-of-focus background in the densely-labeled brain of CaMPKII-GCaMP6s mouse [27]. These results demonstrate that AO correction is crucial for accurate recording of the neuronal and dendritic activities through the thinned-skull window.

Microglia, the brain-resident phagocytes, play a critical role in brain homeostasis and neurological diseases. The resting microglia with motile processes are highly sensitive to subtle changes in brain parenchyma, and they can become activated rapidly with substantial changes in morphology and function upon brain damage or injury [28]. Therefore, minimally invasive imaging tools with the ability to resolve the fine processes are crucial for the study of microglial physiology in the native environment. Taking advantage of our approach, we conducted *in vivo* imaging of Cx3Cr1-GFP mice with microglia labeled with green fluorescent protein (GFP). We first examined whether the thinned-skull (50 μm thickness) preparation triggered the inflammatory response of microglia using time-lapse imaging. Here, ramification and surveillance of the microglial processes were quantified and monitored following the thinned-skull surgery to evaluate the potential surgical effect on microglia activation [29]. As indicated by the ramified morphology and surveying behavior (Fig. S9 in Ref. [21]), the microglia were not activated, and the "thick" thinned-skull window effectively protected underlying brain tissue. By virtue of the fast AO correction (Table S1 in Ref. [21]), we sequentially measured and corrected the aberrations in each subvolume and then stitched them together to form a mosaic image of large FOV. As can be seen, after full AO correction, the branching processes of microglia can be visualized clearly across the entire FOV 400 μm below the pia [Figs. 2(f) and 2(g)].

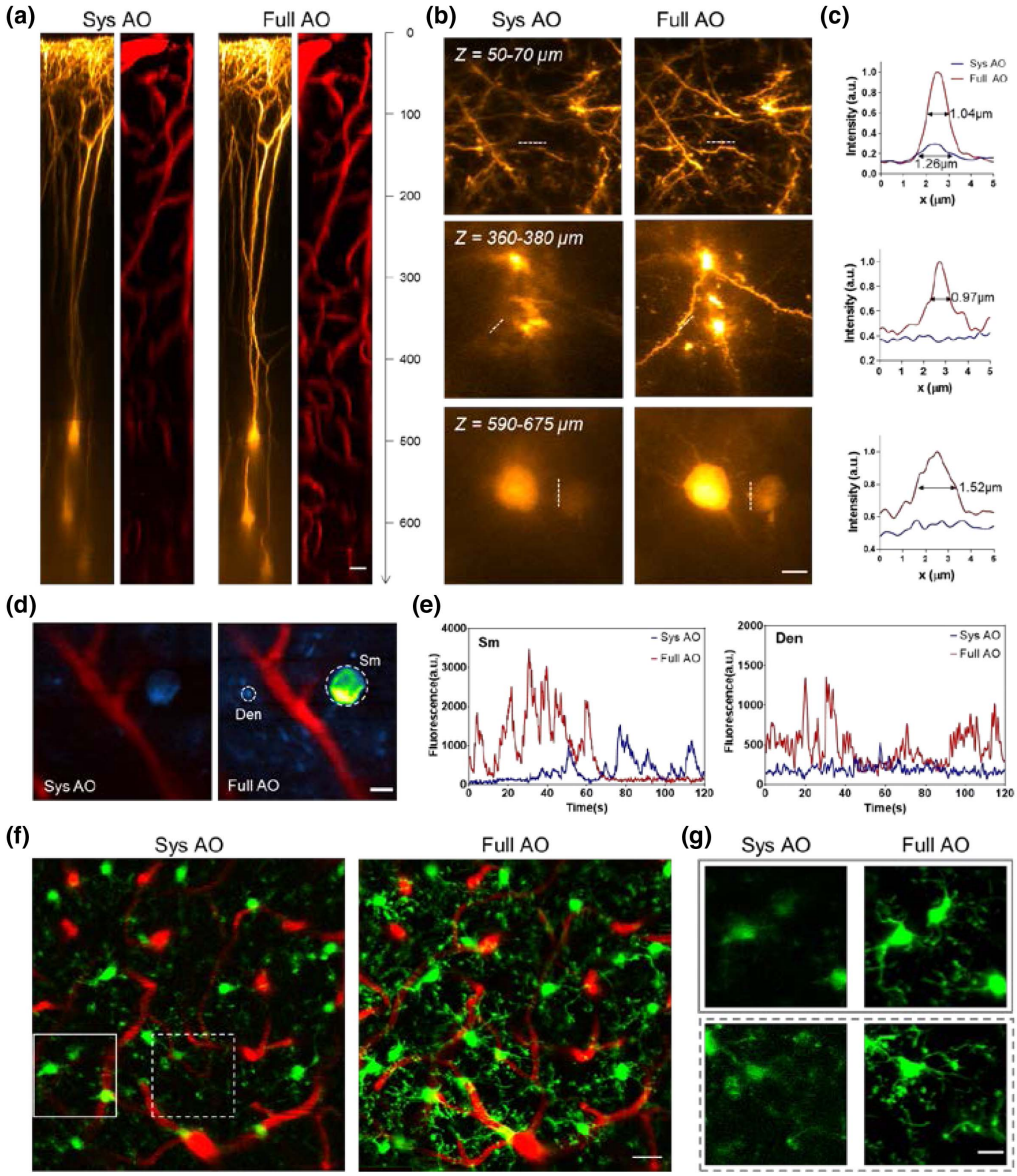

Fig. 2. AO improves structural and functional brain imaging *in vivo* through the thinned-skull window. (a) *xz* maximum-intensity projection (MIP) images of the pyramidal neurons (orange) and microvasculature (red) in Thy1-YFP mice through a thinned-skull window (50 μm in thickness) with system correction only (left) and full AO correction (right). AO corrections was performed every 50 μm of depth. Similar results were performed at 5 sites from 4 mice, for a total $n = 5$. Scale bar: 20 μm. (b) *xy* MIP of the stack images in (a). Scale bar: 5 μm. (c) Intensity profiles along the dashed lines in (b) with system (blue) and full (red) AO corrections. Lateral resolutions were estimated in terms of full width at half-maximum (FWHM). (d) *In vivo* imaging of spontaneous activity of neurons and dendrites in the somatosensory cortex of the CaMPK-GCaMP6s mice under light anesthesia. The neurons are shown as standard-deviation (STD) projections of 600 frames recorded at 340 μm below the pia with only system correction (left) or with full AO correction (right). Similar results for $n = 6$. Scale bar: 10 μm. (e) Fluorescence traces for the soma (Sm) and dendrites (Den) as indicated by the dashed circles in (d). Background fluorescence measured from the nearby vessel location was subtracted from the fluorescence signal. (f) *In vivo* imaging of microglia (green) and microvessels (red) at 350–400 μm below the pia in the Cx3Cr1-GFP mice with system (left) and full (right) AO corrections. Full AO corrections were performed every 40 μm, and 5 × 5 subregions were stitched together to form the entire image. Similar results for $n = 5$. Scale bar: 20 μm. (g) Magnified views of the boxed region in (d). Scale bar: 10 μm.

C. High-Resolution Imaging of Microglia–Plaque Interaction and High-Precision Laser Surgery

By using our AO two-photon microscopy, we can perform high-resolution transcranial imaging in deep cortical layers without interrupting the brain homeostasis, which is crucial for the study of microglial roles with laminar characteristics under certain pathological conditions. For example, we investigated the microglial activity in the AD mice brain, which has a laminar distribution of amyloid plaques [30]. We observed significant morphological and functional differences between the plaque-associated and plaque-distant microglia in layer II/III of mice cortex [Figs. 3(a) and 3(b)]. While the plaque-distant microglia have highly ramified processes with

similar motility as that in the normal brain, the microglia surrounding the amyloid plaques show less ramified morphologies with no obvious dynamics [Fig. 3(b)]. These results indicate that normal microglia may undergo phenotype alteration that is associated with the layer-specific distribution of amyloid plaque during the progression of AD pathology. Our AO-assisted minimally invasive imaging method can also facilitate the therapeutic study on the microglia-mediated inflammation in AD.

Laser microsurgery, because of its high spatial precision of injury, has become a valuable tool for studying the cellular mechanisms that underlie various pathological phenomena such as neuronal degeneration and vascular disruption [31–34]. However, high-precision laser surgery through skull windows is challenging because of large distortion of laser focus. We then applied the AO approach to study microglia–neuron interactions following laser-mediated neuronal injury through a thinned-skull window in Cx3Cr1-GFP/Thy1-YFP mice. We specifically targeted the first bifurcation point of the primary apical dendrite of a layer 5 pyramidal neuron and its neighboring compartments [Fig. 3(c)]. As shown in Figs. 3(d) and 3(e), the microglial processes and neuronal dendrites/spines were clearly visualized using full AO correction. More importantly, AO also enabled precise laser microsurgery through the thinned-skull window, allowing us to ablate the branch point without influencing the nearby neurites, which is impossible otherwise. Time-lapse imaging revealed that the activation of microglia was highly correlated with the degeneration of the injured neuron {Figs. 3(f) and 3(g), Fig. S10 in Ref. [21]}. While the local microglia near the injured site extended their processes rapidly toward the ablation point and completely wrapped around it within 10 min, microglia further away (either upper or deeper) also showed coordinated responses to the neuronal degeneration as indicated by decreased process motility {Figs. 3(f) and 3(g), Fig. S10 in Ref. [21], and Visualization 1}. In addition, we also performed laser dendrotomy on a tuft dendrite of the layer 5 pyramidal neuron and high-precision single spine ablation without damaging the

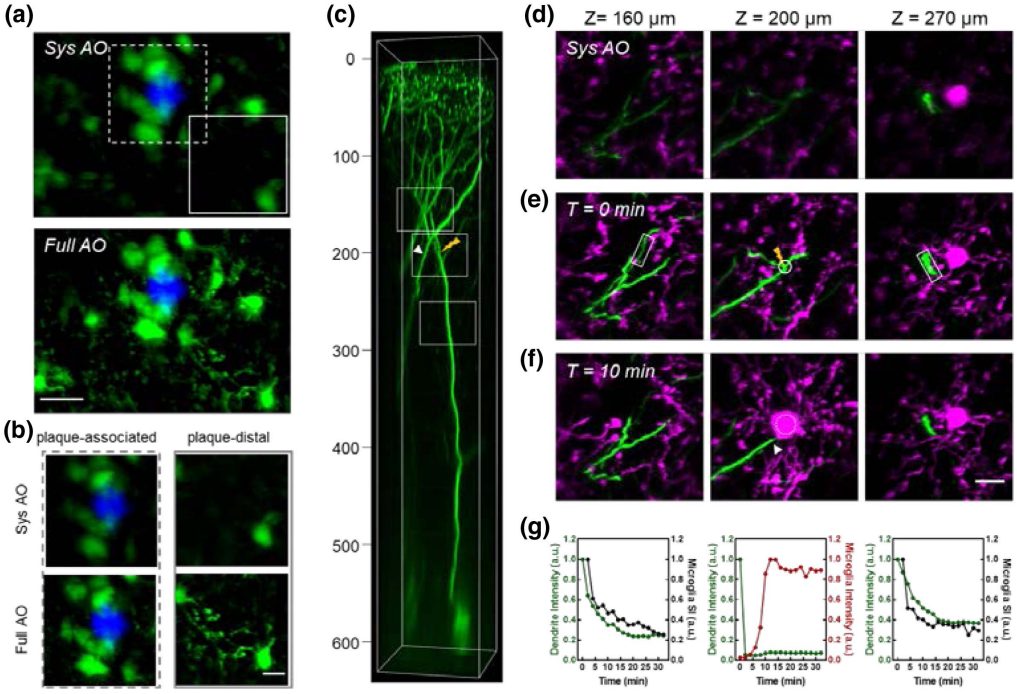

Fig. 3. Study of microglial activities in AD mice and neuron–microglial interactions following precise laser micro-lesion. (a) *In vivo* imaging of amyloid plaque (blue) and microglia (green) at 230–270 μm below the pia in the APP-PS1/Cx3Cr1-GFP mice through a thinned-skull window with system (top) and full (bottom) AO corrections. Full AO correction was performed every 40 μm, and 3 × 3 subregions were stitched together to form the entire image. Amyloid plaque was labeled by MeO-X04 through intraperitoneal injection. Similar results for $n = 3$. Scale bar: 20 μm. (b) Magnified views of the boxed region in (a) showing the plaque-associated (left) and plaque-distal (right) microglia. Scale bar: 10 μm. (c) 3D reconstruction of pyramidal neurons in Thy1-YFP/Cx3Cr1-GFP mice through a thinned-skull window with full AO correction. Similar results for $n = 2$. (d) and (e) *xy* MIP images of neuronal dendrites (green) and microglia (magenta) of the boxed region in (c) with (d) system and (e) full AO corrections before laser ablation. Imaging depths: left column, $Z = 140$–180 μm; middle column, $Z = 180$–220 μm; right column, $Z = 250$–290 μm. The bifurcation point of the apical dendrite ($Z = 200$ μm) was targeted for laser microsurgery [thunder symbol in (c) and middle panel of (e)]. The rectangular boxes in the left and right panels of (e) indicate the distal and proximal end of the apical dendrite of the targeted neuron, respectively. (f) Full AO corrected images taken 10 min after laser ablation. The persistence of neurites of a nearby intact neuron [arrowhead in (c) and the middle plane of (f)] indicates the confinement of the laser injury. Scale bar: 10 μm. (g) Characterization of microglial response to the dendritic degeneration. Left and right: microglial surveillance index (black line) and fluorescence decay (green line) of the distal and proximal dendrites [boxed region in the left and right panel of (e)]; middle: influx of microglial processes to the injured spots represented by the microglial fluorescence intensity [dotted circle in the middle panel of (f)] and the fluorescence decay of the injured dendrite [solid circle in the middle panel of (e)].

dendritic shaft and nearby spines, which resulted in distinct microglial responses (Fig. S11 in Ref. [21] and Visualization 2). Although there is a chance that nearby unlabeled brain structures were injured, the removal of a single spine without influencing the parent dendrite indicates the submicrometer precision of AO-assisted laser microsurgery. These results demonstrated the great potential of AO for precise optical manipulation, in addition to high-resolution imaging.

D. Cortical Imaging at High Resolution through the Optical Clearing Skull Window

The optical clearing skull window is another technique for minimally invasive imaging of the brain [8–10]. By degrading the collagens and inorganic minerals with chemical reagents, the scattering of the mouse skull can be reduced greatly, enabling *in vivo* imaging of the underlying cortex without disturbing brain homeostasis {Fig. 4(a), Figs. S12 and S13 in Ref. [21]}. However, although the fluorescence intensity was enhanced tremendously after optical clearing, the imaging contrast and spatial resolution were still low because of the skull-induced aberration [Fig. 4(a)]. Following the study of AO imaging through thinned-skull window, we sought to explore whether our AO approach could also improve imaging performance through optical clearing windows. The *in vitro* imaging results showed that despite the large aberration caused by the heterogeneity of skull and refractive index mismatch between the clearing reagents and water, our AO approach can recover the optimal spatial resolution effectively up to 500 μm below the skull (Fig. S14 in Ref. [21]). *In vivo* imaging of the mouse cortex through the cleared-skull window of 70 μm thickness shows that AO improved the imaging

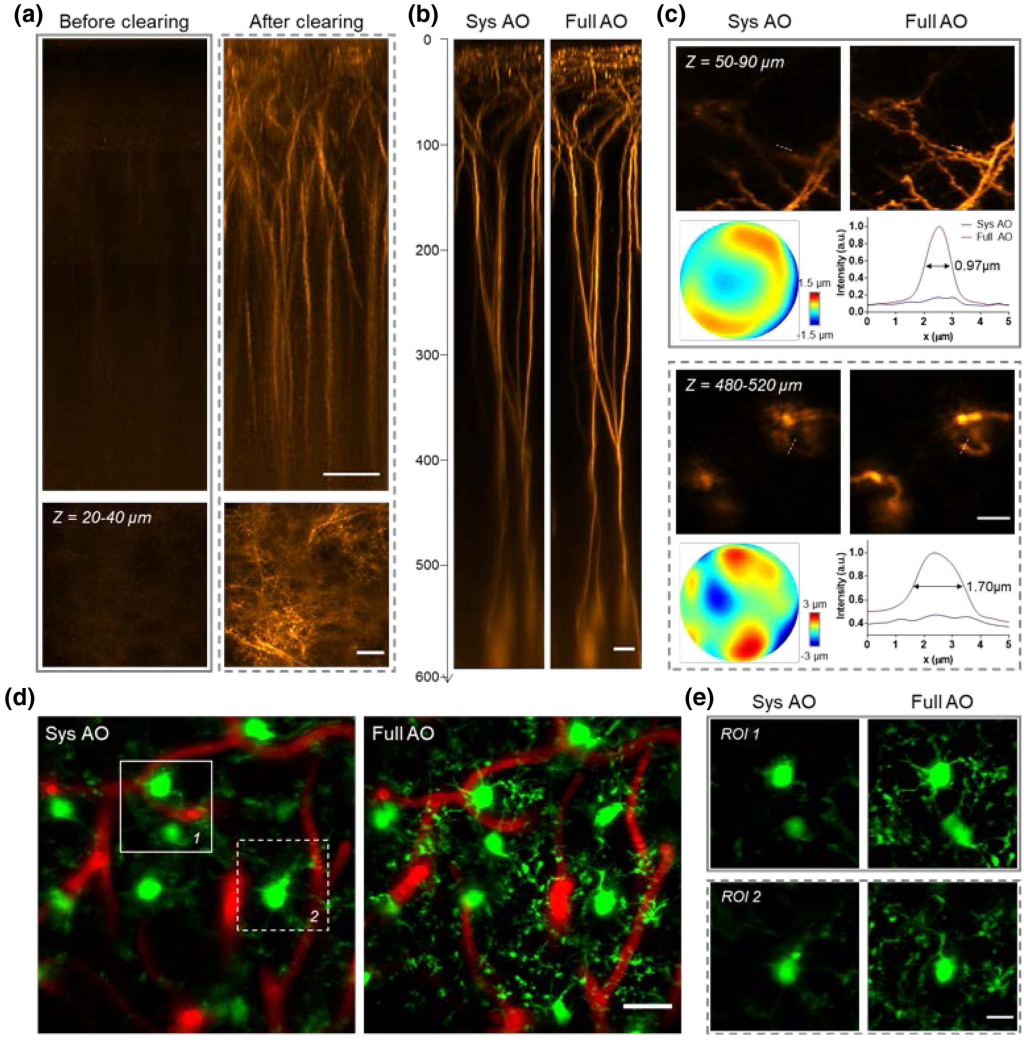

Fig. 4. AO recovers high-resolution imaging of the cortex through an optical clearing window. (a) *xz* MIP of two-photon images of the YFP labelled neurons in the six-week-old Thy1-YFP mice before (left) and after (right) optical clearing. Scale bar: 50 μm. Bottom row shows the *xy* MIP of the stack images. Similar results for $n = 3$. Scale bar: 20 μm. (b) *xz* MIP images of the pyramidal neurons in Thy1-YFP mice through the optical clearing window with system (left) and full (right) AO corrections. AO correction was performed at every 50 μm depth. Scale bar: 20 μm. (c) *xy* MIP of the stack images in (b) at two representative depths and the corresponding corrective wavefront and intensity profiles along the dashed lines. Scale bar: 10 μm. (d) *In vivo* imaging of microglia (green) and microvessels (red) at 175–225 μm below the pia in the Cx3Cr1-GFP mice with system (top) and full (bottom) AO corrections. Full AO corrections were performed every 40 μm, and 3 × 3 subregions were stitched together to form the entire image. Similar results for $n = 3$. Scale bar: 20 μm. (e) Magnified views of images of the boxed regions in (d). Scale bar: 10 μm.

resolution and fluorescence brightness up to 600 μm below the pia [Figs. 4(b) and 4(c)]. Further, the branching processes of microglia can also be visualized clearly with AO correction [Figs. 4(d) and 4(e)], which allows us to study the dynamics of microglial processes in both physiological and pathological conditions. It should be noted that the imaging depth of the optical clearing skull window is smaller than that of the thinned-skull preparation, likely due to the larger skull-induced scattering.

3. DISCUSSION

Two-photon microscopy in conjunction with a cranial window preparation has become the method of choice for *in vivo* brain imaging of small rodents in the past years. While the open-skull approach allows long-term chronic access to the brain, the accompanied inflammatory effects hinder its applications in neuroscience research, especially for immune-associated studies [35]. *In vivo* imaging through intact skull is an ideal noninvasive approach and has been demonstrated by using three-photon excitation. However, strong aberration and scattering of the intact skull will degrade the spatial resolution significantly with increased imaging depth [36,37]. The less invasive thinned-skull window is a much preferred alternative for two-photon microscopy, but the skull-induced scattering and aberrations severely degrade the imaging performance. In this work, we advanced the imaging system and AO technique for high-resolution deep-brain imaging through minimally invasive skull windows. We optimized the excitation NA of our microscope system and developed a wavefront processing algorithm to improve the accuracy of wavefront sensing. In particular, the reduced effective NA for excitation and wavefront sensing has three benefits: (1) the bad Shack–Hartmann spots beyond the aperture of reduced NA are rejected, (2) the deformable mirror can be fully utilized to produce accurate correction for the aberrations, and (3) the TPEF signals are enhanced up to twofold due to the reduced scattering of excitation light. By averaging the guide star signals over a 3D subvolume, asymmetry of Shack–Hartmann spots caused by the highly inhomogeneous microstructure of tissue can be effectively reduced, leading to much improved wavefront sensing. We achieved *in vivo* morphological imaging of layer 5 pyramidal neurons up to 700 μm below pia as well as functional calcium imaging of neuronal activities at high spatial resolution and sensitivity through the thinned-skull window. Further, by taking advantage of the optimal PSF provided by AO correction, we performed precise laser ablation of a single dendrite or spine and studied the interaction between neurites and microglial cells following neuronal microsurgery. Our results demonstrate that AO promises to advance the minimally invasive imaging tools and facilitate neuroscience research in the living brain.

Because of the extreme optical inhomogeneity of skull bone, the aberration varies quickly at different focal positions, and the optimal corrective FOV is 30–60 μm for the thinned-skull and optical clearing skull windows, which are smaller than that of the open-skull cranial window (100–150 μm [15,16,38]). Thanks to fast AO correction by direct wavefront sensing (2–20 s, Table S1 in Ref. [21]), we measured the aberrations sequentially for each subvolume and stitched these subimages together to form an image of an entire large FOV. We have demonstrated that by using our approaches, direct wavefront sensing enabled high-resolution cortical imaging up to 700 μm below the pia through a thinned-skull window. The imaging resolution and contrast in deeper brain regions are still compromised by the dominant scattering caused by the skull and brain tissue. In this case, longer excitation/emission wavelengths and even three-photon absorption process are preferred [36,39]. In conjunction with emerging NIR fluorescent agents such as quantum dots and organic conjugated polymer dots [40,41], direct-wavefront-sensing-based AO technology holds the potential to improve three-photon imaging through the thinned-/cleared-skull and intact-skull windows.

4. MATERIALS AND METHODS

A. Adaptive Optics Two-Photon Microscopy

A schematic diagram of our microscopy system is shown in Fig. S1 in Ref. [21]. The 2P excitation beam (920 nm) from a tunable mode-locked femtosecond laser (Chameleon Ultra II, Coherent) was expanded and collimated by a pair of achromatic lenses to slightly overfill the aperture of the DM (DM97-15, Alpao). The reflected beam with shaped wavefront was then compressed by a $4f$ telescope formed by two VIS-NIR achromatic doublets L5 and L6 (49-365 and 49-794, Edmunds) to match the aperture of a Galvo X scan mirror, which was conjugated with the DM. The Galvo XY-scan mirrors (6215H, Cambridge Technology) were mutually conjugated through a $4f$ relay formed by L7 and L8, both of which consist of two doublets (49-392, Edmunds). The Galvo Y and the rear pupil of the water-immersive objective (XLPLN25XSVMP2, 25×, 1.05 NA, and 2 mm working distance, Olympus) were then conjugated by the scan lens L9 and the tube lens L10 operating in the $4f$ relay configuration. Two groups of scan/tube lens combinations with magnification 3.33-fold or 2.25-fold were chosen to overfill or underfill the objective. For the overfilled condition, L9 consists of two doublets (49-391, Edmunds) and L10 is doublets (49-393, Edmund); for the underfilled condition, L9 consists of two doublets (49-392, Edmunds) and L10 is changed to doublets (49-365, Edmund). The objective was mounted on a motorized linear actuator (LNR50SEK1, Thorlabs) for axial sectioning. For specific imaging conditions requiring two excitation wavelengths simultaneously, another excitation beam (800 nm) from a tunable mode-locked femtosecond laser (Mira 900, Coherent) was integrated into the microscope system via a polarizing beam splitter. The system can operate in two modes: two-photon imaging and wavefront sensing.

For two-photon imaging, the epifluorescence collected by the objective was reflected by a dichroic beam splitter D2 (FF757-Di01-25×36, Semrock) and directed to the photon detection unit. An interchangeable dichroic beam splitter D3 (FF560-Di01-25×36 or FF518-Di01-25×36, Semrock) was inserted at 45° to the beam path to separate the fluorescence into two current photomultiplier (PMT) modules (H11461-03 and H11461-01, Hamamatsu). Two band-pass filters F2 (HQ675/50M, Chroma or FF01-525/50, Semrock) and F3 (FF01-525/50 or FF03-447/60, Semrock) were placed before the PMTs to

select the wavelength bands of the fluorescence. The PMTs' currents were then converted to voltage by two transimpedance amplifiers (SR570, Stanford Research and DLPCA-200, Femto) and subsequently fed into a multifunction data acquisition device (PCIe-6353, National Instrument). Custom-written C# software running in Visual Studio (Microsoft) was used to control the scanner/actuator and to acquire the TPEF images.

For wavefront sensing, the fluorescence emission from the guide star is transmitted through another dichroic beam splitter (Di02-R488-25×36, Semrock) replacing the D2 and then descanned by Galvo XY mirrors. The fluorescence signal was then reflected by the DM and separated from the excitation laser by the dichroic beam splitter D1 (FF705-Di01-25×36, Semrock), before being relayed by a lens pair L9 and L10 (AC254-200-A and AC254-100-A, Thorlabs) to the microlens array (18-00197, SUSS MicroOptics) of the SHWS. The SHWS camera (iXon Ultra 888, Andor) was placed at the focal plane of the microlens array to record the pattern of spots of the fluorescent guide star, enabling direct measurement of its wavefront distortion. A band-pass filter F1 (HQ675/50M, Chroma or FF01-525/50, Semrock) was put before the SHWS to select the wavelength of the guide star signal. It should be noted that the DM, Galvo X and Y mirrors, rear pupil of the objective, and microlens array of the SHWS were all mutually conjugated. The DM and SHWS were operated in a closed-loop configuration and controlled by a custom MATLAB program integrated with the C# imaging software.

B. Calibration of the DM

DM calibration following the previous procedure described by Wang was conducted before it was integrated into the imaging system [15]. Briefly, the influence function of each DM actuator was measured using a Michelson interferometer. The actuators' driving voltages for the first 65 Noll's Zernike modes were then obtained using the measured influence functions. After calibration, the DM can take any desired shape using a linear combination of these Zernike modes.

C. System AO Correction

Before any imaging experiment, the aberrations induced by the optical imperfections in the microscope system were corrected based on a sensorless AO algorithm [38]. In brief, the TPEF intensity of a fluorescent dye (rhodamine 6G) was used as a feedback signal to optimize the DM shape pattern. Seven to nine different values for each Zernike mode were applied sequentially to the DM, and the corresponding intensity of fluorescence was fitted to a Gaussian function to determine the optimum value for each Zernike mode. The first 21 Zernike modes (tip, tilt, and defocus excluded) were used in the optimization cycle to determine and compensate for the system aberration $\boldsymbol{Z}_{\text{sys}}$. The system AO correction mainly consists of low-order aberrations and only needs to be done once before experiments. Therefore, we choose the simple intensity-based optimization algorithm to correct for the system imperfections, though it is relatively time consuming. For *in vivo* imaging experiments, we employed a high-sensitivity SHWS for rapid and robust correction of sample-induced aberrations, which will be described in the following sections.

D. Calibration of the SHWS

The SHWS was calibrated with the DM in the microscope system as described previously [17]. Briefly, the nonlinear guide star signals from the fluorescent dye solution were descanned and used for AO calibration of the DM and SHWS in a closed-loop configuration. The first 65 Zernike modes with root-mean-square c_i and $-c_i$ were applied sequentially to the DM, and the corresponding spot patterns $\boldsymbol{S}_i^+ = (x_1 \cdots x_N, y_1 \cdots y_N)$ and $\boldsymbol{S}_i^-$ on the SHWS were recorded, where (x_j, y_j) represents the center location of the jth spot. Then the influence matrix $\boldsymbol{M}_{sz}$ of the DM to SHWS can be acquired, where

$$\boldsymbol{M}_{sz} = \begin{bmatrix} (\boldsymbol{S}_1^+ - \boldsymbol{S}_1^-)/2c_1 \\ \vdots \\ (\boldsymbol{S}_{65}^+ - \boldsymbol{S}_{65}^-)/2c_{65} \end{bmatrix}.$$

Each row of $\boldsymbol{M}_{sz}$ represents the shift (x and y) of the spots on the SHWS to each Zernike mode. The 65 rows in the influence matrix $\boldsymbol{M}_{sz}$ form the calibration basis for subsequent AO correction.

E. Full AO Correction

Full AO correction compensates for both system- and sample-induced aberrations. First, the DM was set to correct the system aberration $\boldsymbol{Z}_{\text{sys}}$ obtained using the sensorless method mentioned above. The TPEF signal of rhodamine at the FOV center creates a reference spot pattern on the SHWS $\boldsymbol{S}_{\text{Sref}} = (x_1 \cdots x_N, y_1 \cdots y_N)$. To measure and correct the sample-induced aberration, a small FOV within the sample was scanned by the excitation laser to create a descanned and integrated wavefront on the SHWS. The SHWS images were first cross-correlated with a Gaussian function that equals the PSF of the microlens, and then the centroids of each spot were determined using a center of mass algorithm with an iterative window size [42], allowing high-precision, robust estimation even for asymmetric spot patterns. The reliability weight of each spot depends on its SBR $\boldsymbol{W} = \text{Diag}(w_1 \cdots w_N, w_1 \cdots w_N)$. The spot's displacement from the reference pattern $\boldsymbol{S}_{\text{Sref}}$ calculated as $\Delta\boldsymbol{S} = \boldsymbol{S}_{\text{all}} - \boldsymbol{S}_{\text{Sref}}$ represents the sample-induced wavefront distortion. Then the additional corrective pattern of the DM can be computed by minimizing the total aberration as follows:

$$\begin{aligned} \Delta\boldsymbol{Z} &= \arg\min_{\Delta\boldsymbol{Z}} \| \boldsymbol{W}^{1/2}(\boldsymbol{M}_{sz}\Delta\boldsymbol{Z} + \Delta\boldsymbol{S}) \|_2^2 \\ &= -(\boldsymbol{M}_{SZ}^T \boldsymbol{W} \boldsymbol{M}_{SZ})^{-1} \boldsymbol{M}_{SZ}^T \boldsymbol{W} \Delta\boldsymbol{S}. \end{aligned}$$

Then we added the correction of sample-induced aberration back to the system correction to achieve the full AO correction: $\boldsymbol{Z}_{\text{full}} = \boldsymbol{Z}_{\text{sys}} + \Delta\boldsymbol{Z}$, which corrects aberrations induced by both sample and system. Although the wavefront measurement is based on the emission wavelength and not the excitation wavelength, the chromatic effects have negligible influence on the performance of AO correction, which has been also reported in the previous work [13,14]. Note that all the corrective wavefronts shown in this work represent the corrections for sample-induced aberrations.

F. Monte Carlo Simulation

Nonsequential mode Zemax software was used for Monte Carlo simulation of photon propagation through brain tissue,

skull window, and the optical system of wavefront sensing (Fig. S2a in Ref. [21]). The brain tissue and skull window were modeled as a semi-infinite scattering volume of optical properties for brain tissue (10 mm × 10 mm × 10 mm) covered by a 50 μm thick plate of optical properties for skull (10 mm × 10 mm × 0.05 mm). The Henyey–Greenstein scattering model was employed to define the angular scattering of the rays. The scattering coefficients of brain tissue and skull at wavelength of 520 nm were 13 mm^{-1} and 30 mm^{-1}, with anisotropy value of 0.88 and 0.92, respectively [43]. An ellipsoid volume source (semi-axis lengths: 0.5, 0.5, 5 μm) that emitted photons randomly and isotopically was embedded in the "brain tissue" to model the two-photon excited fluorescent guide star. The size of the light source was close to the PSF measured using fluorescent beads at 300 μm depth below the skull with system correction only. The emitted photons were collected by an ideal water-immersion lens with NA of 1.05, which resembled the objective lens. The back focal plane of the objective, DM, and lens array were mutually conjugated by a $4f$ telescope system like our AO TPEF microscope system. A rectangular detector was placed at the focal plane of the lens array to capture the simulated Shack–Hartmann spots. To simulate the overfilled and underfilled conditions with different effective NAs, the magnification ratio between objective and DM was chosen accordingly, and the DM surface acted as an aperture to reject rays from higher angle that entered the objective. The total number of photons hitting the detector of the SHWS was kept approximately same at different NA configurations. The same Zernike aberrations were applied to the DM surface so that the measured aberrations were independent from NA. To calculate the wavefront errors, we used the aberrations reconstructed by the SHWS images without scattering (by setting the scattering coefficient of brain and skull to 0) as the ground truth. And the relative wavefront error was defined as $\frac{\|Z_{sc}-Z_{nsc}\|^2}{\|Z_{nsc}\|^2} \times 100\%$, where Z_{sc} and Z_{nsc} are the aberrations measured by the SHWS with and without scattering, respectively.

G. Direct Wavefront Sensing by Line Scanning along the Microvessels in a 3D Subvolume

To measure aberrations at depth, we employed the two-photon excited NIR guide star from Evans blue in the microvessels over a small 3D volume. In detail, we first programmed the scanners to sequentially scan the blood vessel segments in an imaging plane of small FOV (~60 μm × 60 μm) with a scanning rate of ~10 Hz. The descanned fluorescent guide star signals were integrated on an EMCCD camera to form the SHWS image. The integration time was chosen to yield an SHWS image of good signal-to-noise ratio, and the chosen integration times under different measurement conditions are summarized in Table S1 in Ref. [21]. It should be noted that the passage of red blood cells or the blood flow only affects the integration time of SHWS image but not the wavefront measurement. To perform the average of guide star signals over a 3D volume, we recorded the SHWS images at two or more adjacent planes (depth range <60 μm) (Figs. S7c and S7d in Ref. [21]). As can been seen, a large number of spots with irregular and asymmetrical patterns appear in each raw SHWS image, producing errors in wavefront measurement and aberration correction (Figs. S7c and S7d in Ref. [21]). Next, we averaged the SHWS images acquired from the planes at different adjacent depths and found that the complex irregular and asymmetrical patterns were tremendously reduced in most cells of the SHWS (Fig. S7e in Ref. [21]), and the spatial-variant high-order wavefront distortions were largely cancelled out. When the center of a lenslet spot is still unidentifiable (e.g., SBR <3 used in our experiments [16]) after 3D averaging, the signal in the corresponding cell of the SHWS image was spatially filtered with its four nearest neighboring cells of 1/4 weight. Overall, we found that the wavefront reconstruction algorithm with the combination of 3D averaging and neighboring filtering yielded high-quality SHWS images to identify the focal spot in each cell, allowing more accurate determination of the averaged aberrations in the highly heterogeneous tissue (Fig. S7f in Ref. [21]).

H. Animal Preparation

Five transgenic mouse lines, Thy1-YFP [Tg(Thy1-YFP)HJrs/J] [44], Cx3Cr1-GFP [B6.129P2(Cg)-Cx3cr1^{tm1Litt}/J] [45], Thy1-YFP/Cx3Cr1-GFP, APP-PS1/Cx3Cr1-GFP, and CaMPKII-GCaMP6s mice were used in this study. Thy1-YFP/Cx3Cr1-GFP mice were generated by crossing Thy1-YFP mice with Cx3Cr1-GFP mice, and APP-PS1/Cx3Cr1-GFP mice were obtained by crossing APP-PS1 [Tg(APPswe, PSEN1dE9)85Dbo] mice with Cx3Cr1-GFP mice. CaMPKII-GCaMP6s mice were generated by crossing CaMPKII-Cre [Tg (Camk2a-cre)T29-1Stl] mice with GCaMP6s-Dio [Ai162 (TIT2L-GC6s-ICL-tTA2)-D] mice. All the animal procedures conducted in this work followed an animal protocol approved by the Animal Ethics Committee of HKUST.

Mice (>6 weeks) were anesthetized by intraperitoneal (i.p.) injection of ketamine/xylazine mixture (10 μL/g) before surgery. After the skull was exposed by performing a midline scalp incision, a scalpel was used to remove gently the periosteum attached to the skull. Then a custom-designed rectangular head plate with a circular hole was centered on the right hemisphere and sealed onto the skull by applying a small amount of cyanoacrylate adhesive to the perimeter of the hole. Dental acrylic was then applied to the exposed skull surface to fill the gap between the head plate and skull. After the dental acrylic became dry and hard, the mice were mounted on a head-holding stage with angle adjusters (NARISHIGE, MAG-2) and placed under a stereomicroscope for surgical preparation of either a thinned-skull or optical-cleared skull window.

Thinned-skull window. The thinned-skull preparation is slightly modified from a previous protocol [4]. Briefly, a 500 μm carbon steel burr attached to a rotatory high-speed drill was used to gently thin a circular region (2.0–2.5 mm in diameter) with the center at stereotactic coordinate (3 mm, 3 mm) laterally and posterior to the bregma point. After removing the majority of the middle spongy bone, a microsurgical blade (No. 6961, Surgistar) was used to carefully thin the skull further to about 40–50 μm. Surface irregularities were reduced by occasionally changing the thinning direction of the surgical blade. Finally, a biocompatible sealant mixture (Kwik-Cast, WPI), which can be peeled off before the imaging experiment, was applied to cover the thinned-skull window.

Optical cleared skull window. The reagents used for optically clearing the skull include: 10% EDTA disodium (D2900000, Sigma-Aldrich), 80% glycerol (G5516, Sigma-Aldrich), and USOCA (consists of S1 and S2) [8–10]. S1 is prepared by dissolving urea (Sinopharm, China) in 75% ethanol at a 10:3 volume-mass ratio. S2 is a sodium dodecylbenzenesulfonate (SDBS) prepared by mixing NaOH solution (0.7 mol/L) with dodecylbenzenesulfonic acid (DDBSA, Aladdin) at a 24:5 volume-mass ratio. The skull optical clearing procedure follows the method described in previous reports [8–10]. Briefly, the exposed skull was first treated with S1 for about 20 min, with a clean cotton swab gently rubbing the skull surface to accelerate the clearing process. Then the S1 was removed using a cotton ball and replaced with S2 for a further 5 min. After the S2 was removed, 10% EDTA was dropped onto the skull for another 20 min and then replaced with 80% glycerol. Finally, a thin layer of plastic wrap was used to cover the cleared skull to separate the immersion medium (water) from glycerol during *in vivo* imaging.

I. *In vivo* Imaging

Mice were anesthetized and received a retro-orbital intravenous injection of Evans blue (10 μg/g; E2129, Sigma-Aldrich) before imaging to label the lumen of blood vessels. The APP-PS1/Cx3Cr1-GFP mice were also i.p. injected with MeO-X04 (5.0 mg/kg, 10% DMSO, 90% PBS) 2 h before imaging to label amyloid deposits in the brain. Before fluorescence imaging, the skull window was aligned precisely perpendicular to the objective axis by adjusting the angles of the head-holding stage guided by second-harmonic generation imaging of bone collagen.

For two-photon structural imaging of neurons (YFP), microglia (GFP), and blood vessels (Evans blue), the animal was anesthetized with ketamine/xylazine mixture. The femtosecond laser was tuned to 920 nm, and the post-objective excitation power ranged from 20 to 200 mW depending on the imaging depth. To image amyloid plaques in the APP-PS1/Cx3Cr1-GFP mice, another femtosecond laser tuned to 800 nm was used to excite the MeO-X04 fluorescence with an incident power of less than 30 mW at the skull surface. The system aberrations for the 800 and 920 nm lasers were calibrated individually because they did not share the same optical path (Fig. S1a in Ref. [21]). For *in vivo* imaging, after the measurement of sample-induced aberrations, the full AO corrections for the two lasers are calculated as described in Section 4.E by adding the correction of sample-induced aberration to the system corrections. The system or full AO correction patterns for the 800 and 920 nm lasers are updated on the DM accordingly when one of lasers was used as the excitation.

For two-photon calcium imaging, the animal was under light anesthesia (0.5% isoflurane), and the 920 nm laser for GCaMP6s excitation has an optical power less than 200 mW at the skull surface. For wavefront sensing, the nonlinear fluorescence guide star was created by scanning the 920 nm laser over a small FOV (30 μm × 30 μm) or selectively choosing a small vessel via multiple line scanning. Detailed imaging and wavefront sensing parameters are listed in Table S1 in Ref. [21].

J. Laser-Mediated Microsurgery

To perform precise and efficient microsurgery using the femtosecond laser, the sample-induced aberration for the ablation site was first measured and compensation applied. For laser dendrotomy, a 920 nm laser with an average power of 400 mW was focused on the dendritic shaft for 1–2 s, the actual exposure time being controlled by the feedback signal of newly created fluorescence during the multiphoton ionization process [46,47]. For single spine ablation, a 920 nm laser with an average power of 200–300 mW was focused on the dendritic spine for 2 s.

K. Spectral Unmixing of GFP and YFP Signal

We used Thy1-YFP/Cx3Cr1-GFP mice to study the interaction between neurons and microglia. Because the emission spectra of YFP and GFP are very close, we designed a simple algorithm using a linear model to distinguish the two components. To image GFP and YFP, D3 was replaced with dichroic beam splitter FF518-Di01-25X36, and F2 and F3 were both the band-pass filters FF01-525/50 (Fig. S1 in Ref. [21]). Therefore, the detection bands of the two PMT channels are 518–550 nm and 500–518 nm, respectively, corresponding to the emission peaks of YFP and GFP. Assuming that the fluorescence brightnesses of YFP and GFP at the imaging location are C_Y and C_G, and the detected signal intensities of PMT1 and PMT2 are I_1 and I_2, we have the following equations:

$$\begin{bmatrix} I_1 \\ I_2 \end{bmatrix} = \begin{bmatrix} w_{1,1} & w_{1,2} \\ w_{2,1} & w_{2,2} \end{bmatrix} \begin{bmatrix} C_Y \\ C_G \end{bmatrix} = \begin{bmatrix} w_1 & 1 \\ 1 & w_2 \end{bmatrix} \begin{bmatrix} \alpha C_Y \\ \beta C_G \end{bmatrix}.$$

The parameters w_1 and w_2 can be calibrated from the image locations where only YFP-labelled neurons or GFP-labelled microglia exist. The unmixed normalized signal intensity for YFP and GFP can be represented by αC_Y and βC_G, where

$$\begin{bmatrix} \alpha C_Y \\ \beta C_G \end{bmatrix} = \begin{bmatrix} w_1 & 1 \\ 1 & w_2 \end{bmatrix}^{-1} \begin{bmatrix} I_1 \\ I_2 \end{bmatrix}.$$

By using this method, we can unmix the fluorescence signal of YFP-labelled neurons and GFP-labelled microglia.

L. Image Analysis

The images were processed in MATLAB (Mathworks) or ImageJ (NIH) [48]. Several algorithms for image registration were used to mitigate motion artefacts depending on the level of the animal motion itself. For most imaging conditions when the animal motion was negligible, only a single frame was captured per slice for the stack images. The stack images were registered using the rigid-body transformation provided by the stackreg plugin [49] in ImageJ. When animal motion became apparent and inter-frame artefacts appeared, the imaging speed was increased and several frames were acquired per slice for the whole stack images (Table S1 in Ref. [21]). Image registration was performed on sequential frames for each slice using the turboreg plugin [49] in ImageJ to correct the rigid motion artefact, or with the hidden Markov model algorithm [50] to correct within-frame motion artefacts.

For mosaiced images of microglia and blood vessels, multitile subimages were captured with predefined positions and then stitched together to form the mosaic image using the Grid/Collection Stitching [51] plugin in ImageJ.

Funding. Hong Kong University of Science and Technology (RPC10EG33); Area of Excellence Scheme of the University Grants Committee (AOE/M-09/12, AoE/M-604/16); Innovation and Technology Commission (ITCPD/17-9); Research Grants Council, University Grants Committee (16102518, 16103215, 16148816, 662513, C6001-19E, C6002-17GF, N_HKUST603/19, T13-605/18W, T13-607/12R, T13-706/11-1).

Acknowledgment. We thank Jufang He and Peng Tang from City University of Hong Kong for providing the CaMPKII-GCaMP6s transgenic mice, and Dongyu Li from Huazhong University of Science and Technology for useful discussions and support regarding the optical clearing experiments.

Disclosures. All authors declare that they have no competing interests.

Data Availability. All data presented in this paper and/or the supplementary materials are available upon reasonable request from the corresponding author.

[†]These authors contributed equally to this paper.

REFERENCES

1. F. Helmchen and W. Denk, "Deep tissue two-photon microscopy," Nat. Methods **2**, 932–940 (2005).
2. K. Svoboda and R. Yasuda, "Principles of two-photon excitation microscopy and its applications to neuroscience," Neuron **50**, 823–839 (2006).
3. A. Holtmaat, T. Bonhoeffer, D. K. Chow, J. Chuckowree, V. De Paola, S. B. Hofer, M. Hübener, T. Keck, G. Knott, W.-C. A. Lee, R. Mostany, T. D. Mrsic-Flogel, E. Nedivi, C. Portera-Cailliau, K. Svoboda, J. T. Trachtenberg, and L. Wilbrecht, "Long-term, high-resolution imaging in the mouse neocortex through a chronic cranial window," Nat. Protoc. **4**, 1128–1144 (2009).
4. G. Yang, F. Pan, C. N. Parkhurst, J. Grutzendler, and W.-B. Gan, "Thinned-skull cranial window technique for long-term imaging of the cortex in live mice," Nat. Protoc. **5**, 201–208 (2010).
5. H.-T. Xu, F. Pan, G. Yang, and W.-B. Gan, "Choice of cranial window type for in vivo imaging affects dendritic spine turnover in the cortex," Nat. Neurosci. **10**, 549–551 (2007).
6. R. D. Dorand, D. S. Barkauskas, T. A. Evans, A. Petrosiute, and A. Y. Huang, "Comparison of intravital thinned skull and cranial window approaches to study CNS immunobiology in the mouse cortex," Intravital **3**, e29728 (2014).
7. C. Chen, Z. Liang, B. Zhou, X. Li, C. Lui, N. Y. Ip, and J. Y. Qu, "*In vivo* near-infrared two-photon imaging of amyloid plaques in deep brain of Alzheimer's disease mouse model," ACS Chem. Neurosci. **9**, 3128–3136 (2018).
8. Y.-J. Zhao, T.-T. Yu, C. Zhang, Z. Li, Q.-M. Luo, T.-H. Xu, and D. Zhu, "Skull optical clearing window for *in vivo* imaging of the mouse cortex at synaptic resolution," Light Sci. Appl. **7**, 17153 (2018).
9. C. Zhang, W. Feng, Y. Zhao, T. Yu, P. Li, T. Xu, Q. Luo, and D. Zhu, "A large, switchable optical clearing skull window for cerebrovascular imaging," Theranostics **8**, 2696–2708 (2018).
10. Y. Chen, S. Liu, H. Liu, S. Tong, H. Tang, C. Zhang, S. Yan, H. Li, G. Yang, D. Zhu, K. Wang, and P. Wang, "Coherent Raman scattering unravelling mechanisms underlying skull optical clearing for through-skull brain imaging," Anal. Chem. **91**, 9371–9375 (2019).
11. M. J. Booth, "Adaptive optical microscopy: the ongoing quest for a perfect image," Light Sci. Appl. **3**, e165 (2014).
12. N. Ji, "Adaptive optical fluorescence microscopy," Nat. Methods **14**, 374–380 (2017).
13. R. Aviles-Espinosa, J. Andilla, R. Porcar-Guezenec, O. E. Olarte, M. Nieto, X. Levecq, D. Artigas, and P. Loza-Alvarez, "Measurement and correction of *in vivo* sample aberrations employing a nonlinear guide-star in two-photon excited fluorescence microscopy," Biomed. Opt. Express **2**, 3135–3149 (2011).
14. K. Wang, D. E. Milkie, A. Saxena, P. Engerer, T. Misgeld, M. E. Bronner, J. Mumm, and E. Betzig, "Rapid adaptive optical recovery of optimal resolution over large volumes," Nat. Methods **11**, 625–628 (2014).
15. K. Wang, W. Sun, C. T. Richie, B. K. Harvey, E. Betzig, and N. Ji, "Direct wavefront sensing for high-resolution *in vivo* imaging in scattering tissue," Nat. Commun. **6**, 7276 (2015).
16. R. Liu, Z. Li, J. S. Marvin, and D. Kleinfeld, "Direct wavefront sensing enables functional imaging of infragranular axons and spines," Nat. Methods **16**, 615–618 (2019).
17. Z. Qin, S. He, C. Yang, J. S.-Y. Yung, C. Chen, C. K.-S. Leung, K. Liu, and J. Y. Qu, "Adaptive optics two-photon microscopy enables near-diffraction-limited and functional retinal imaging in vivo," Light Sci. Appl. **9**, 79 (2020).
18. D. Débarre, E. J. Botcherby, T. Watanabe, S. Srinivas, M. J. Booth, and T. Wilson, "Image-based adaptive optics for two-photon microscopy," Opt. Lett. **34**, 2495–2497 (2009).
19. N. Ji, D. E. Milkie, and E. Betzig, "Adaptive optics via pupil segmentation for high-resolution imaging in biological tissues," Nat. Methods **7**, 141–147 (2010).
20. J. Tang, R. N. Germain, and M. Cui, "Superpenetration optical microscopy by iterative multiphoton adaptive compensation technique," Proc. Natl. Acad. Sci. USA **109**, 8434–8439 (2012).
21. More figures and tables supporting this work are available at https://doi.org/10.6084/m9.figshare.14658870.v1.
22. M. Gu, T. Tannous, and J. R. Sheppard, "Effect of an annular pupil on confocal imaging through highly scattering media," Opt. Lett. **21**, 312–314 (1996).
23. E. Beaurepaire and J. Mertz, "Epifluorescence collection in two-photon microscopy," Appl. Opt. **41**, 5376–5382 (2002).
24. M. Kondo, K. Kobayashi, M. Ohkura, J. Nakai, and M. Matsuzaki, "Two-photon calcium imaging of the medial prefrontal cortex and hippocampus without cortical invasion," eLife **6**, e26839 (2017).
25. N. Ji, T. R. Sato, and E. Betzig, "Characterization and adaptive optical correction of aberrations during *in vivo* imaging in the mouse cortex," Proc. Natl. Acad. Sci. USA **109**, 22–27 (2012).
26. W. Göbel and F. Helmchen, "*In vivo* calcium imaging of neural network function," Physiology **22**, 358–365 (2007).
27. P. Theer and W. Denk, "On the fundamental imaging-depth limit in two-photon microscopy," J. Opt. Soc. Am. A **23**, 3139–3149 (2006).
28. C. N. Parkhurst and W.-B. Gan, "Microglia dynamics and function in the CNS," Curr. Opin. Neurobiol. **20**, 595–600 (2010).
29. C. Madry, V. Kyrargyri, I. L. Arancibia-Cárcamo, R. Jolivet, S. Kohsaka, R. M. Bryan, and D. Attwell, "Microglial ramification, surveillance, and interleukin-1β release are regulated by the two-pore domain K^+ channel THIK-1," Neuron **97**, 299–312 (2018).
30. R. A. Armstrong, "Original article Laminar distribution of β-amyloid (Aβ) peptide deposits in the frontal lobe in familial and sporadic Alzheimer's disease," Folia Neuropathol. **1**, 15–23 (2015).
31. L. Sacconi, R. P. O'Connor, A. Jasaitis, A. Masi, M. Buffelli, and F. S. Pavone, "*In vivo* multiphoton nanosurgery on cortical neurons," J. Biomed. Opt. **12**, 050502 (2007).
32. A. J. Canty, L. Huang, J. S. Jackson, G. E. Little, G. Knott, B. Maco, and V. De Paola, "*In-vivo* single neuron axotomy triggers axon regeneration to restore synaptic density in specific cortical circuits," Nat. Commun. **4**, 2038 (2013).
33. N. Nishimura, C. B. Schaffer, B. Friedman, P. S. Tsai, P. D. Lyden, and D. Kleinfeld, "Targeted insult to subsurface cortical blood vessels using ultrashort laser pulses: three models of stroke," Nat. Methods **3**, 99–108 (2006).
34. A. Y. Shih, P. Blinder, P. S. Tsai, B. Friedman, G. Stanley, P. D. Lyden, and D. Kleinfeld, "The smallest stroke: occlusion of one penetrating vessel leads to infarction and a cognitive deficit," Nat. Neurosci. **16**, 55–63 (2013).
35. T. L. Roth, D. Nayak, T. Atanasijevic, A. P. Koretsky, L. L. Latour, and D. B. McGavern, "Transcranial amelioration of inflammation and cell death after brain injury," Nature **505**, 223–228 (2014).

36. T. Wang, D. G. Ouzounov, C. Wu, N. G. Horton, B. Zhang, C.-H. Wu, Y. Zhang, M. J. Schnitzer, and C. Xu, "Three-photon imaging of mouse brain structure and function through the intact skull," Nat. Methods **15**, 789–792 (2018).
37. Y. Wang, M. Chen, N. Alifu, S. Li, W. Qin, A. Qin, B. Z. Tang, and J. Qian, "Aggregation-induced emission luminogen with deep-red emission for through-skull three-photon fluorescence imaging of mouse," ACS Nano **11**, 10452–10461 (2017).
38. J.-H. Park, L. Kong, Y. Zhou, and M. Cui, "Large-field-of-view imaging by multi-pupil adaptive optics," Nat. Methods **14**, 581–583 (2017).
39. D. M. Chow, D. Sinefeld, K. E. Kolkman, D. G. Ouzounov, N. Akbari, R. Tatarsky, A. Bass, C. Xu, and J. R. Fetcho, "Deep three-photon imaging of the brain in intact adult zebrafish," Nat. Methods **17**, 605–608 (2020).
40. O. T. Bruns, T. S. Bischof, D. K. Harris, D. Franke, Y. Shi, L. Riedemann, A. Bartelt, F. B. Jaworski, J. A. Carr, C. J. Rowlands, M. W. B. Wilson, O. Chen, H. Wei, G. W. Hwang, D. M. Montana, I. Coropceanu, O. B. Achorn, J. Kloepper, J. Heeren, P. T. C. So, D. Fukumura, K. F. Jensen, R. K. Jain, and M. G. Bawendi, "Next-generation *in vivo* optical imaging with short-wave infrared quantum dots," Nat. Biomed. Eng. **1**, 0056 (2017).
41. S. Wang, J. Liu, G. Feng, L. G. Ng, and B. Liu, "NIR-II excitable conjugated polymer dots with bright NIR-I emission for deep *in vivo* two-photon brain imaging through intact skull," Adv. Funct. Mater. **29**, 1808365 (2019).
42. P. M. Prieto, F. Vargas-Martín, S. Goelz, and P. Artal, "Analysis of the performance of the Hartmann–Shack sensor in the human eye," J. Opt. Soc. Am. A **17**, 1388–1398 (2000).
43. S. L. Jacques, "Optical properties of biological tissues: a review," Phys. Med. Biol. **58**, R37–R61 (2013).
44. G. Feng, R. H. Mellor, M. Bernstein, C. Keller-Peck, Q. T. Nguyen, M. Wallace, J. M. Nerbonne, J. W. Lichtman, and J. R. Sanes, "Imaging neuronal subsets in transgenic mice expressing multiple spectral variants of GFP," Neuron **28**, 41–51 (2000).
45. S. Jung, J. Aliberti, P. Graemmel, M. J. Sunshine, G. W. Kreutzberg, A. Sher, and D. R. Littman, "Analysis of fractalkine receptor CX_3CR1 function by targeted deletion and green fluorescent protein reporter gene insertion," Mol. Cell Biol. **20**, 4106–4114 (2000).
46. Q. Sun, Z. Qin, W. Wu, Y. Lin, C. Chen, S. He, X. Li, Z. Wu, Y. Luo, and J. Y. Qu, "*In vivo* imaging-guided microsurgery based on femtosecond laser produced new fluorescent compounds in biological tissues," Biomed. Opt. Express **9**, 581–590 (2018).
47. Z. Qin, Q. Sun, Y. Lin, S. He, X. Li, C. Chen, W. Wu, Y. Luo, and J. Y. Qu, "New fluorescent compounds produced by femtosecond laser surgery in biological tissues: the mechanisms," Biomed. Opt. Express **9**, 3373–3390 (2018).
48. J. Schindelin, I. Arganda-Carreras, E. Frise, V. Kaynig, M. Longair, T. Pietzsch, S. Preibisch, C. Rueden, S. Saalfeld, B. Schmid, J.-Y. Tinevez, D. J. White, V. Hartenstein, K. Eliceiri, P. Tomancak, and A. Cardona, "Fiji: an open-source platform for biological-image analysis," Nat. Methods **9**, 676–682 (2012).
49. P. Thévenaz, U. E. Ruttimann, and M. Unser, "A pyramid approach to subpixel registration based on intensity," IEEE Trans. Image Process. **7**, 27–41 (1998).
50. P. Kaifosh, M. Lovett-Barron, G. F. Turi, T. R. Reardon, and A. Losonczy, "Septo-hippocampal GABAergic signaling across multiple modalities in awake mice," Nat. Neurosci. **16**, 1182–1184 (2013).
51. S. Preibisch, S. Saalfeld, and P. Tomancak, "Globally optimal stitching of tiled 3D microscopic image acquisitions," Bioinformatics **25**, 1463–1465 (2009).